Applied Catalysis B: Environmental 87 (2009) 18–29

Contents lists available at ScienceDirect

Applied Catalysis B: Environmental

journal homepage: www.elsevier.com/locate/apcatb

# Reduction of $NO_x$ by $H_2$ on $Pt/WO_3/ZrO_2$ catalysts in oxygen-rich exhaust

F.J.P. Schott, P. Balle, J. Adler, S. Kureti *

*Institut für Technische Chemie und Polymerchemie, Universität Karlsruhe, Kaiserstrasse 12, D-76128 Karlsruhe, Germany*

ARTICLE INFO

*Article history:*
Received 30 June 2008
Received in revised form 19 August 2008
Accepted 26 August 2008
Available online 31 August 2008

*Keywords:*
$NO_x$ reduction
$H_2$
Pt
$WO_3$
$ZrO_2$
Diesel exhaust
Mechanism
DRIFTS

ABSTRACT

This work addresses the low-temperature $NO_x$ abatement under oxygen-rich conditions using $H_2$ as reductant. For this purpose $Pt/ZrO_2$ and $Pt/WO_3/ZrO_2$ catalysts are developed and characterised by temperature-programmed desorption of $H_2$ ($H_2$-TPD), $N_2$ physisorption (BET) and powder X-ray diffraction (PXRD). The most active catalyst is a $Pt/WO_3/ZrO_2$ pattern with a Pt load of 0.3 wt.% and a W content of 11 wt.%. This material reveals high de$NO_x$ activity below 200 °C and high overall $N_2$ selectivity of about 90%. Additionally, the catalyst exhibits outstanding hydrothermal stability as well as resistance against $SO_x$. Furthermore, the transfer from the powder level to real honeycomb systems leads to promising performance as well.

Diffuse reflectance Fourier transform infrared spectroscopic studies, kinetic modelling of temperature-programmed desorption of $O_2$ ($O_2$-TPD) and $NO_x$-TPD examinations indicate that the pronounced $H_2$-de$NO_x$ performance of the $Pt/WO_3/ZrO_2$ catalyst is related to the electronic interaction of $WO_3$ with the precious metal. The tungsten promoter increases the electron density on the Pt thus activating the sample for $H_2$-de$NO_x$ and $N_2$ formation, respectively. Contrary, $NO_x$ surface species formed on the $WO_3/ZrO_2$ support are not supposed to be involved in the $H_2$-de$NO_x$ reaction.



## 1. Introduction

Nitrogen oxides ($NO_x$) emitted by lean-burn engines contribute to various environmental problems, for instance formation of acid rain as well as ozone. As a consequence, the emission limits have been worldwide tightened in the past. For the removal of $NO_x$ from oxygen-rich exhaust the selective catalytic reduction (SCR) using $NH_3$ and $NO_x$ storage reduction catalyst (NSR) are currently the most favoured technologies. However, a serious constraint of these techniques is the minor de$NO_x$ performance below 200 °C. Contrary, the catalytic reduction of $NO_x$ by $H_2$ ($H_2$-de$NO_x$) reveals an interesting potential for the low-temperature $NO_x$ abatement being particularly crucial for diesel passenger cars. In the driving cycle of the European Union the exhaust temperature is below 150 °C for about 60% of cycle time. Thus, SCR and NSR do not cover the most part of the certification cycle and might therefore come under pressure when the exhaust limits will be markedly tightened in the future. This clearly indicates the need for a de$NO_x$ technique operating at low temperatures. Furthermore, low-temperature $NO_x$ reduction exhibits a potential for industrial applications as well, e.g. for fossil power plants, waste combustion plants, nitric acid production and air separation.

First published in 1971 Jones et al. show the effective $NO_x$ reduction by $H_2$ in slight excess of $O_2$ using a $Pt/Al_2O_3$ catalyst [1]. High $NO_x$ conversions are observed between 65 and 200 °C while indicating a high yield of nitrous oxide as well; at maximum de$NO_x$ the molar ratio of $N_2/N_2O$ is shown to be unity. The mechanism of the reaction of NO with $H_2$ on $Pt/Al_2O_3$ involves the reduction of the active Pt sites by $H_2$ followed by adsorption and dissociation of NO [2]. The recombination of two N atoms leads to the formation of $N_2$, whereas the oxygen is retained onto the Pt surface. Contrary, $N_2O$ is produced by combination of a N atom and NO being adsorbed on neighbouring Pt sites.

In the last years some Pt $H_2$-de$NO_x$ catalysts are presented revealing considerable low-temperature activity even under strongly oxidising conditions [3–6]. Wildermann reports on a very active $Pt/Al_2O_3$ catalyst that shows maximum performance already at 70 °C [3]. However, this material produces a huge proportion of $N_2O$ being in line with the results from Jones et al. [1]. For example, at peak $NO_x$ conversion the $N_2O$ selectivity amounts to 80%. Moreover, Wildermann indicates the enhancement of activity and $N_2$ production of $Pt/Al_2O_3$ by using the promoter Mo (3.4 wt.%) resulting in a $N_2$ selectivity of 40%. The performance of this $Pt/Mo/Al_2O_3$ catalyst is additionally enhanced by Co, whereas the $N_2$ selectivity is slightly increased only. However, the activity

* Corresponding author. Tel.: +49 721 608 8090; fax: +49 721 608 2816.
*E-mail address:* kureti@ict.uni-karlsruhe.de (S. Kureti).

0926-3373/$ – see front matter © 2008 Elsevier B.V. All rights reserved.
doi:10.1016/j.apcatb.2008.08.021

declines when CO exceeds 0.15 vol.% [7,8] being in accordance with Lambert and Macleod [9,10].

Costa et al. report a $Pt/La_{0.7}Sr_{0.2}Ce_{0.1}FeO_3$ catalyst with pronounced low-temperature activity as well as substantially increased $N_2$ selectivity up to 80–90% [11,12]. Detailed examinations performed with a related $Pt/La_{0.5}Sr_{0.2}Ce_{0.51}MnO_3$ sample [12] indicate a different reaction mechanism as compared to that elucidated for $Pt/Al_2O_3$ [2]. Costa et al. postulate chemisorption of $NO_x$ on the support resulting in nitro and nitrato surface species, while $H_2$ adsorbs dissociatively on the Pt component. Then, the atomic hydrogen spills over to the support reducing the $NO_x$ surface complexes to release $N_2$ and $H_2O$. Following Costa et al. this mechanism suppresses the formation of $N_2O$. A very similar mechanism is postulated for a $Pt/MgO–CeO_2$ catalyst being very active as well [13,14]. In contrast to platinum, Ru, Ir, Rh, Pd and Ag [3,15] as well as perovskite catalysts [11,16–18] reveal no or at least low performance in excess of $O_2$. An exception is $Pd/LaCoO_3$ showing considerable activity [19]. Furthermore, it is worth mentioning that the $H_2$-de$NO_x$ reaction is an important feature of the TWC technology as well as in regeneration of NSR catalysts reducing $NO_x$ under stoichiometric and rich conditions, respectively.

The aim of this paper is the development of a $H_2$-de$NO_x$ catalyst showing both pronounced low-temperature activity and minimum $N_2O$ production, whereas the present study mainly focuses on diesel exhaust. For this purpose a series of $Pt/ZrO_2$ and $Pt/WO_3/ZrO_2$ samples is systematically prepared, characterised and finally tested for $H_2$-de$NO_x$. These systems are selected as a result of pre-studies in which different support materials have been screened [20,21], e.g. $Al_2O_3$, $SiO_2$, $ZrO_2$, $TiO_2$ and MgO carriers all modified with alkaline and alkaline earth metals, elements of the 1st period of transition metals, Ce, La and Mo. For the evaluation of the technical potential of the most promising catalyst relevant conditions are varied, while a coated honeycomb is employed as well. Additionally, mechanistic examinations are performed to gain insight into the effectiveness of the best catalyst.

## 2. Experimental

### 2.1. Development of the $ZrO_2$ support and catalyst preparation

Preliminary catalytic investigations show that the synthesis route, crystalline phase and BET surface area of the $ZrO_2$ substrate strongly affect the performance of the $H_2$-de$NO_x$ catalysts [22]. The best result is obtained with a self-prepared zirconia existing in the tetragonal phase. This material is synthesised by advancing the so-called hydrazine route [23,24] providing reliable product quality and sufficient mass to coat several full size honeycombs for automotive applications. For the synthesis a solution of 234 g $ZrO(NO_3)_2$ (Fluka) in 1.6 l distilled $H_2O$ is added to a boiling mixture of 400 ml $N_2H_4{\cdot}H_2O$ (Fluka) and 1.2 l distilled $H_2O$. The resulting blend is digested for 12 h under reflux, whereas shorter reaction time leads to unwanted monoclinic $ZrO_2$ as well (Fig. 1). After filtration and washing with $H_2O$ the solid is dried overnight at 100 °C and calcined in air at 750 °C for 6 h. The yield of $ZrO_2$ is almost 100% (85 g).

The introduction of Pt is carried out by incipient wetness method. In this impregnation a defined volume of $Pt(NO_3)_2$ (Chempur) solution is taken such that it is completely absorbed by the substrate. The adjusted Pt loads referring to the support range from 0.1 to 2.0 wt.%. After impregnation, the samples are dried overnight at 100 °C and are then activated by dosing a gas mixture of 9 vol.% $H_2$ and 91 vol.% $N_2$. In the activation step the temperature is increased from 20 to 300 °C at the rate of 1.0 K $min^{-1}$; the end temperature is held for 30 min. Finally, the samples are conditioned by heating in air at 500 °C for 5 h. For reference purposes a classical $Pt/Al_2O_3$ catalyst is also prepared taking commercially available γ-$Al_2O_3$ balls ($d$ = 0.6 mm, Sasol).

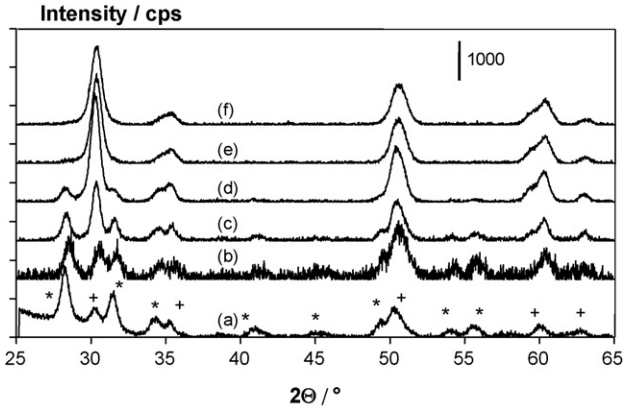


**Fig. 1.** PXRD patterns of the prepared $ZrO_2$ support depending on the digestion time (a) 5 min, (b) 1 h, (c) 4 h, (d) 7 h, (e) 12 h and (f) 17 h; * monoclinic phase; + tetragonal phase); final calcination is performed in air at 750 °C for 6 h; analytical parameters of PXRD are described in next section.

The modification of $ZrO_2$ with tungsten is performed by incipient wetness method as well using a solution of $(NH_4)_6H_2W_{12}O_{41}$ (Fluka). Different loads of W (up to 22 wt.%) relating to the mass of $ZrO_2$ are established by varying the concentration of $(NH_4)_6H_2W_{12}O_{41}$. After impregnation, the sample is dried overnight at 100 °C and is then impregnated by Pt as mentioned above. It is worth noting that in the $H_2$ activation tungsten oxide is not reduced [24].

### 2.2. Characterisation of the catalysts

Crystalline phase of the pure supports as well as catalysts is examined by powder X-ray diffraction (PXRD). The PXRD patterns are recorded at room temperature on a Siemens D 501 using Ni filtered Cu Kα radiation. A 2$\theta$ step size of 0.02° is used with an integration time of 4 s. The diffractogram of the commercial $Al_2O_3$ carrier confirms the γ-modification, while the prepared $ZrO_2$ is in the tetragonal phase as already demonstrated in Fig. 1. Regardless of the load of W no reflexes of crystalline tungsten oxide are observed suggesting amorphous $WO_x$ domains, at least at W contents above 6 wt.% when tungsten oxide exists in sufficient abundance to be monitored. Additionally, signals of Pt are not found as well being associated with its low contents.

The dispersion of Pt is studied by temperature-programmed desorption of $H_2$ ($H_2$-TPD). In these analyses, same laboratory bench is used as in the catalytic investigations (Section 2.4). Respective sample (1.5 g) is charged into the quartz glass tube reactor (i.d. 8 mm) and pre-treated in Ar flow at 600 °C for 15 min. Subsequently, the catalyst is cooled to 300 °C and exposed to a gas mixture of 5 vol.% $H_2$ and 95 vol.% Ar for 30 min to reduce the active Pt surface. The pattern is then rapidly cooled to 30 °C in the $H_2$/Ar flow. After saturation, it is flushed with Ar and $H_2$-TPD is started using Ar as carrier gas (100 ml $min^{-1}$, STP). In TPD the catalyst is heated to 600 °C at the rate of 20 K $min^{-1}$, whereupon temperature is recorded by a K type thermocouple (TC) fitted directly in front of the sample. Desorbing $H_2$ is continuously monitored by thermal conductivity detection (TCD, Shimadzu). For specific analysis of $H_2$ the reactor effluents pass a cold trap (−50 °C) removing $H_2O$. The Pt dispersion ($d_{Pt}$) is determined by supposing that one H adsorbs per active Pt site (Eq. (1)) [25]. The molar amount of desorbing $H_2$ ($n_{H_2}$) is obtained by integrating the corresponding TCD signal, whereas the total proportion of Pt ($n_{Pt}$) is known from the impregnation procedure.

**Table 1**
Load of Pt and W, sample code, BET surface area and Pt dispersion of the $H_2$-de$NO_x$ catalysts

| Catalyst system | m(Pt) (%) | m(W) (%) | Sample code | $S_{BET}$ ($m^2\,g^{-1}$) | $d_{Pt}$ (%) |
|---|---|---|---|---|---|
| $Pt/Al_2O_3$ | 0.5 | | $0.5Pt/Al_2O_3$ | 150 | 5 |
| | 2 | | $2Pt/Al_2O_3$ | 148 | 9 |
| $Pt/ZrO_2$ | 0.1 | | $0.1Pt/ZrO_2$ | 99 | 30 |
| | 0.3 | | $0.3Pt/ZrO_2$ | 100 | 25 |
| | 0.5 | | $0.5Pt/ZrO_2$ | 100 | 36 |
| | 2 | | $2Pt/ZrO_2$ | 98 | 11 |
| $Pt/WO_3/ZrO_2$[a] | 0.3 | 3 | $0.3Pt/3W/ZrO_2$ | 97 | 36 |
| | 0.3 | 6 | $0.3Pt/6W/ZrO_2$ | 106 | 50 |
| | 0.3 | 11 | $0.3Pt/11W/ZrO_2$ | 68 | 90 |
| | 0.3 | 22 | $0.3Pt/22W/ZrO_2$ | 62 | 95[b] |
| | 2 | 11 | $2Pt/11W/ZrO_2$ | 70 | 11 |

[a] The loads of Pt and W refer to the $ZrO_2$ support.
[b] While the Pt dispersion of $0.3Pt/11W/ZrO_2$ is checked by HRTEM (particles <2 nm), double $H_2$ desorption is observed for $0.3Pt/22W/ZrO_2$. Hence, different H/Pt stoichiometry is assumed being speculated to be 2. This change might be associated with Pt–W interactions dominating at high tungsten oxide coverages amounting to ca. 45% for 22% W.

As derived from blank experiments, e.g. Pt free $11W/ZrO_2$, the $H_2$ desorption is specific for Pt.

$$d_{Pt} = \frac{0.5 n_{H_2}}{n_{Pt}} \quad (1)$$

Furthermore, the $ZrO_2$-based catalyst with a Pt load of 0.3 wt.% and a W content of 11 wt.% is exemplarily characterised by X-ray photoelectron spectroscopy. The spectrometer is a Phoibos 150MCD from Specs being equipped with a Mg anode ($E$(Mg Kα) = 1253 eV). The spectrum shows a clear absorption at 36 eV ($W4f_{7/2}$) being related to $W^{6+}$ species [26].

The BET surface area of the catalysts is investigated by multi-point Sorptomatic 1990 using $N_2$ as adsorbate. The BET data are listed in Table 1 along with the loading, Pt dispersion and sample codes. It is worth mentioning that the declining BET surface area of the $0.3Pt/W/ZrO_2$ samples is mainly related to the increasing proportion of $WO_3$ exhibiting negligible surface area and it is not due to the blocking of pores of the $ZrO_2$ carrier.

### 2.3. $O_2$- and $NO_x$-TPD studies

$O_2$-TPD studies are performed to investigate the kinetics of the adsorption and desorption of $O_2$ on selected catalysts. Oxygen is used as probe molecule since it represents a dominating species on the Pt surface under lean burn conditions [27]. The procedure of $O_2$-TPD is similar to that described above for $H_2$-TPD. The catalyst (5.00 g) is heated in Ar at 750 °C for 15 min, cooled to 50 °C and is then exposed to a mixture of 2 vol.% $O_2$ and 98 vol.% Ar (99.996%, <6 ppm $O_2$) until the sample is saturated. After flushing with Ar (500 ml $min^{-1}$, STP) TPD is started with a rate of 20 K $min^{-1}$. $O_2$ is detected by CIMS (Airsense 500, V & F). As the axial and radial temperature gradients along the catalyst bed are below 10 K heat transfer effects are to be neglected. Furthermore, Mears and Weisz Prater criteria [28], that amount to $10^{-5}$ and $10^{-2}$, respectively, exclude transport limitation by film and pore diffusion.

$NO_x$-TPD examinations are conducted similar to $H_2$-TPD as well using a catalyst mass of 1.50 g. After the pre-treatment performed at 500 °C the sample is cooled to 125 °C in Ar flow and is then exposed to a mixture of 2800 ppm NO and 6 vol.% $O_2$ in Ar. In this treatment NO is partially converted into $NO_2$ (15%) due to catalytic oxidation. After saturation, the dosage of NO and $O_2$ is stopped and the reactor is flushed by Ar followed by starting the TPD with a rate of 20 K $min^{-1}$. Additionally, before beginning the TPD a mixture of (a) 1500 ppm $H_2$, 6 vol.% $O_2$, Ar (balance) or (b) 1500 ppm $H_2$ in Ar is added for 10 min to study the reaction of $NO_x$ surface species with $H_2$. Subsequently, it is purged again and TPD is finally started employing exclusively the CLD analyzer mentioned in the following section.

### 2.4. $H_2$-de$NO_x$ studies

The catalytic investigations are performed on a laboratory bench using a diesel model exhaust. Before the measurements, the samples are pressed to pellet with 40 MPa, granulated and sieved in a mesh size of 125–250 μm; an exception is the $Pt/Al_2O_3$ pattern which is kept in form of balls. The samples (1.50 g) are charged into the quartz glass tube reactor (i.d. 8 mm), fixed with quartz wool and pre-treated in Ar flow at 500 °C for 15 min to remove possible impurities and to provide reproducible conditions. Subsequently, the model exhaust is added and the temperature is decreased to 40 °C with a rate ($\beta$) of 1.0 K $min^{-1}$. Furthermore, some experiments are carried out under stationary conditions at selected temperatures. The standard feed (500 ml $min^{-1}$, STP) is composed of 500 ppm NO, 2000 ppm $H_2$, 6.0 vol.% $O_2$ and Ar as balance. To evaluate the best catalyst the concentration of $H_2$ and $O_2$ is varied and other relevant exhaust gas species, i.e. CO, $H_2O$ and $CO_2$ are dosed additionally. The feed is obtained by blending a special mixture of 2000 ppm $H_2$ and 6.0 vol.% $O_2$ in Ar with the other components (Air Liquide). The flow of each component is controlled by independent mass flow controllers (MKS Instruments), whereas water is supplied by a liquid pump (Kronlab). Temperature is measured by a K type TC located directly in front of and behind the catalyst bed. Using the standard feed the temperature difference between inlet and outlet is below 10 K and therefore only the inlet temperature is presented. The analysis of $NO_x$ is conducted by means of CLD (EL-ht, Eco Physics), while $N_2O$, CO and $CO_2$ are monitored by NDIR spectroscopy (Uras 10 E, Hartmann & Braun). $N_2$ is detected by GC/TCD (RGC 202 with packed columns Haye Sep Q 60 and mol sieve 5 Å, Siemens) resulting in a time resolution of 9 min that corresponds to a temperature interval of 15 K. Oxygen is analysed by using magnetomechanics (Magnos 6 G, Hartmann & Braun).

The $NO_x$ conversion ($X(NO_x)$) refers to the formation of $N_2$ and $N_2O$ as defined by Eq. (2), whereas the temperature programmed $H_2$-de$NO_x$ data are found to be equal to stationary results. For the major part of the reaction the mass of N is balanced being associated with the production of $N_2$ and $N_2O$ thus excluding the genesis of $NH_3$. Nevertheless, below 80 °C $H_2$-de$NO_x$ is slightly interfered by $NO_x$ adsorption corresponding to less than 10% conversion.

$$X(NO_x) = \frac{2c(N_2) + 2c(N_2O)}{c(NO_x)_{in}} \quad (2)$$

The selectivity of $N_2$ ($S(N_2)$) is defined by Eq. (3), whereupon a corresponding expression is used for the $N_2O$ selectivity ($S(N_2O)$). Moreover, for the comparison of different catalysts the overall selectivity of $N_2$ ($S(N_2)_{overall}$) is taken as well (Eq. (4)); $T_1$ and $T_2$ are the temperatures with $NO_x$ conversion of 20%. Selectivity data are exclusively presented for de$NO_x$ above 20% to minimise error propagation.

$$S(N_2) = \frac{c(N_2)}{c(N_2) + c(N_2O)} \quad (3)$$

$$S(N_2)_{overall} = \frac{\int_{T_1}^{T_2} S(N_2)\,dT}{T_2 - T_1} \quad (4)$$

### 2.5. DRIFTS studies

The DRIFT spectroscopic studies are performed with a Nicolet 5700 FTIR spectrometer (Thermo Electron) being equipped with a MCT detector and DRIFTS optics (Thermo Mattson). The sample compartment is continuously purged with $N_2$ to avoid diffusion of air. The IR cell made of stainless steel contains a ZnSe window and is connected to a gas-handling system. The spectra are recorded in the range from 1000 to 4000 $cm^{-1}$ with an instrument resolution of 4 $cm^{-1}$. 100 scans are accumulated to a spectrum resulting in a time resolution of 1 min. Before the analysis, the catalyst powder is charged into the sample holder of the cell and is heated for 30 min at 500 °C in $N_2$ or Ar flow (500 ml $min^{-1}$, STP). In the studies using CO as probe molecule the sample is then exposed at 250 °C for 30 min to a mixture of 2000 ppm $H_2$ and 6 vol.% $O_2$ ($N_2$ balance); this is done to establish similar conditions as in catalytic studies (Section 2.4). Subsequently, the catalyst is cooled in $N_2$ flow to 25 °C and then a background spectrum is recorded. After this, the sample is treated for 5 min with a mixture of 500 ppm CO in $N_2$ followed by purging with $N_2$. Finally, the sample spectrum is collected.

The DRIFTS investigation of $H_2$-deNO$_x$ is performed sequentially. Firstly, the catalyst is cooled from 500 to 125 °C under flowing Ar and then the background spectrum is taken. Subsequently, the sample is exposed for 10 min to a mixture of 1000 ppm NO and 6 vol.% $O_2$ (Ar balance) followed by purging with Ar and taking the spectrum. After this, the blend of 40 or 2000 ppm $H_2$ and 6 vol.% $O_2$ (Ar balance) is added while continuously collecting data. The $H_2$ concentration of 40 ppm is adjusted to definitely avoid hot spots on the catalyst.

The DRIFT spectra are presented in terms of Kubelka Munk transformation defined as $F(R) = (1-R)^2/(2R)$ with $R = R_s/R_r$, whereas $R_s$ is the reflectance of the sample under reaction conditions and $R_r$ that under the Ar flow.

## 3. Results and discussion

### 3.1. Performance of the Pt/$Al_2O_3$ reference and the Pt/$ZrO_2$ catalysts

A preliminary investigation performed in the absence of a catalyst shows no conversion of NO$_x$ excluding $H_2$-deNO$_x$ by gas-phase reactions. In contrast to that, the 0.5Pt/$Al_2O_3$ reference reveals pronounced low-temperature activity, whereas the operation window is rather narrow (50–150 °C) and $N_2O$ forms as the major product; $S(N_2)_{overall}$ amounts to 20% (Fig. 2). The performance of Pt/$Al_2O_3$ is considered to be in fair agreement with literature addressing the same catalytic system [1,3,4].

Fig. 3 illustrates the performance of 0.3Pt/$ZrO_2$ indicating NO$_x$ conversion in the entire temperature range with two deNO$_x$ maxima at 140 and 170 °C. Furthermore, the peak NO$_x$ removal is higher as compared to 0.5Pt/$Al_2O_3$. Another interesting feature is the markedly improved $N_2$ selectivity of 0.3Pt/$ZrO_2$, i.e. $N_2$ is formed as the major product showing an overall selectivity of 55%.

The Pt/$ZrO_2$ samples with Pt contents of 0.1 and 0.5 wt.% show similar peak NO$_x$ conversions of 78 and 82%, respectively, whereas their operation range is restricted covering a range of ca. 140 K only. Furthermore, $S(N_2)_{overall}$ is very similar to 0.3Pt/$ZrO_2$. Hence, the latter material is considered to be superior and is therefore adopted to the Pt/$WO_3$/$ZrO_2$ system. The superiority of 0.3Pt/$ZrO_2$ is difficult to explain as Table 1 shows very similar physical–chemical properties for the Pt/$ZrO_2$ samples.

### 3.2. Performance of the 0.3Pt/W/$ZrO_2$ catalysts

For comparison of the 0.3Pt/W/$ZrO_2$ samples revealing different loads of W the maximum NO$_x$ conversion ($X(NO_x)_{max}$) is used in addition to $S(N_2)_{overall}$. Fig. 4 shows that a little amount of tungsten is sufficient to increase deNO$_x$ as well as $N_2$ selectivity. The optimum content of W is 11 wt.% resulting in an overall $N_2$ selectivity of 85% and a peak NO$_x$ conversion of 95%; assuming planar tungsten oxide the $ZrO_2$ coverage by $WO_3$ is estimated to be 0.22 being significantly less than a monolayer. Furthermore, the results of XPS and PXRD suggest that the tungsten component exists in the form of amorphous $WO_3$.

For clarity the performance of the 0.3Pt/11W/$ZrO_2$ catalyst is presented in Fig. 5. The data point to a broad range of deNO$_x$ with two conversion peaks at 90 and 250 °C. As a consequence, 0.3Pt/11W/$ZrO_2$ covers the low- as well as high-temperature regime thus representing a promising catalytic material. Nevertheless, it should be stated that the low-temperature activity is much more pronounced, while above 250 °C deNO$_x$ declines. The latter feature is attributed to increasing conversion of $H_2$ with $O_2$ being present in excess; a more detailed discussion of the educt selectivity is presented in Section 3.4. The two NO$_x$ conversion maximums are ascribed to different active Pt sites as stated in Section 3.5.3, whereas no evidence for active NO$_x$ species located on the support is found as discussed in Section 3.5.3 as well. Contrary, the bare 11W/$ZrO_2$ support does not directly participate in deNO$_x$ as deduced from a measurement without Pt. However, 0.3Pt/11W/$ZrO_2$ still shows significant formation of $N_2O$ below 150 °C, e.g. at

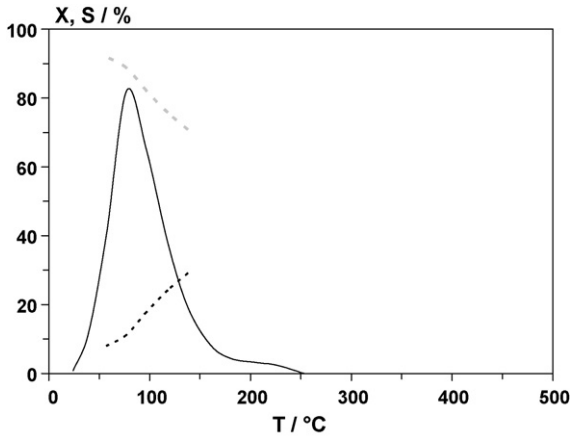


**Fig. 2.** $H_2$-deNO$_x$ performance of 0.5Pt/$Al_2O_3$ ($X(NO_x)$ —, $S(N_2)$ - -, $S(N_2O)$ ▬ ▬). Conditions: $m$ = 1.50 g, $c$(NO) = 500 ppm, $c(H_2)$ = 2000 ppm, $c(O_2)$ = 6.0 vol.%, Ar balance, $F$ = 500 ml $min^{-1}$ (STP), S.V. = 22.000 $h^{-1}$, $\beta$ = 1.0 K $min^{-1}$.

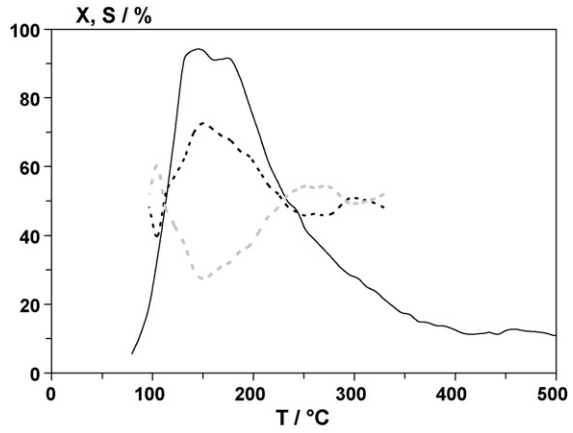


**Fig. 3.** $H_2$-deNO$_x$ performance of 0.3Pt/$ZrO_2$ ($X(NO_x)$ —, $S(N_2)$ - -, $S(N_2O)$ ▬ ▬). Conditions: $m$ = 1.50 g, $c$(NO) = 500 ppm, $c(H_2)$ = 2000 ppm, $c(O_2)$ = 6.0 vol.%, Ar balance, $F$ = 500 ml $min^{-1}$ (STP), S.V. = 22,000 $h^{-1}$, $\beta$ = 1.0 K $min^{-1}$.

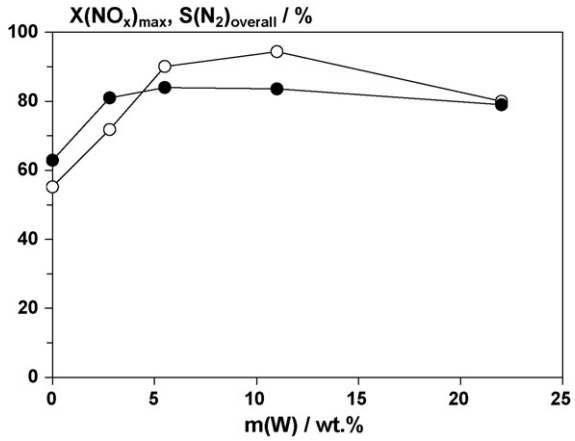


**Fig. 4.** Effect of W load on the $H_2$-de$NO_x$ performance of the 0.3Pt/W/$ZrO_2$ samples ($X(NO_x)_{max}$ ○, $S(N_2)_{overall}$ ●). Conditions: $m$ = 1.50 g, $c$(NO) = 500 ppm, $c(H_2)$ = 2000 ppm, $c(O_2)$ = 6.0 vol.%, Ar balance, $F$ = 500 ml $min^{-1}$ (STP), S.V. = 22.000 $h^{-1}$, $\beta$ = 1.0 K $min^{-1}$.

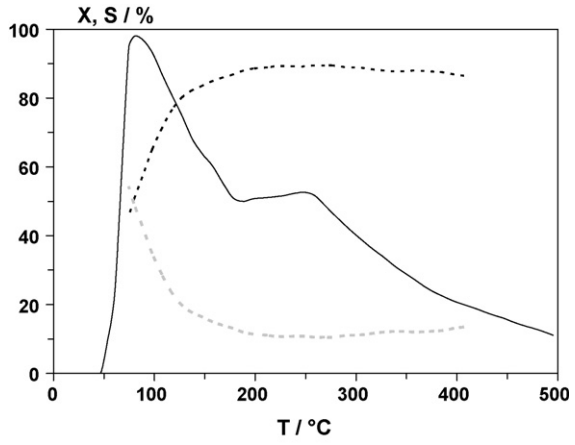


**Fig. 5.** $H_2$-de$NO_x$ performance of 0.3Pt/11W/$ZrO_2$ ($X(NO_x)$ —, $S(N_2)$ - -, $S(N_2O)$ ▬ ▬). Conditions: $m$ = 1.50 g, $c$(NO) = 500 ppm, $c(H_2)$ = 2000 ppm, $c(O_2)$ = 6.0 vol.%, Ar balance, $F$ = 500 ml $min^{-1}$ (STP), S.V. = 22.000 $h^{-1}$, $\beta$ = 1.0 K $min^{-1}$.

the low-temperature de$NO_x$ peak $S(N_2O)$ is about 45%. In contrast to that, $N_2O$ is substantially suppressed above 200 °C corresponding to a $N_2$ selectivity of approximately 90%.

Furthermore, it should be mentioned that no $NH_3$ forms in $H_2$-de$NO_x$ on the 0.3Pt/11W/$ZrO_2$ catalyst as referred from a NDIR analysis (Binos 1.1, Leybold-Heraeus). The suppression of $NH_3$ formation is reported to be typical for $NO_x$ reduction by $H_2$ on Pt catalysts under oxygen-rich conditions [1].

The turnover frequency (TOF) being defined as the number of converted $NO_x$ molecules per Pt atom and time is $8.0 \times 10^{-3}$ $s^{-1}$ for the de$NO_x$ peak at 90% and $5.0 \times 10^{-3}$ $s^{-1}$ for the 250 °C maximum. These specific $H_2$-de$NO_x$ data are very close to that of 0.1Pt/MgO–$CeO_2$ showing a TOF of ca. $8 \times 10^{-3}$ $s^{-1}$ (90 °C) in a similar NO/$H_2$/$O_2$ feed [14]. A direct comparison of the activity range of both catalysts is problematic as data recorded under analogue conditions are not available in the study of 0.1Pt/MgO–$CeO_2$ [14].

### 3.3. Evaluation of the 0.3Pt/11W/$ZrO_2$ catalyst

#### 3.3.1. Effect of $O_2$ and CO on $H_2$-de$NO_x$ performance

The previous section provides evidence that the content of $O_2$ is a crucial parameter for the $H_2$-de$NO_x$ reaction. Hence, the

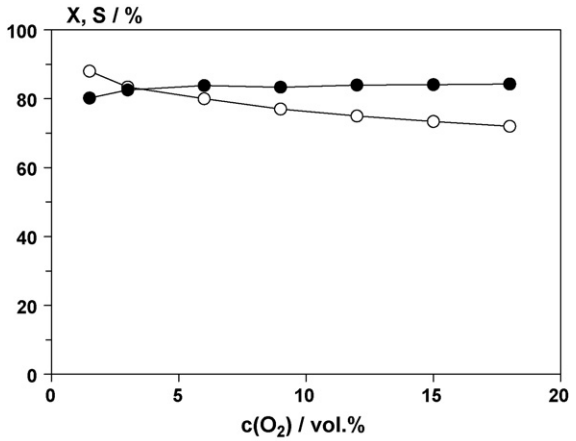


**Fig. 6.** Effect of $O_2$ on the $H_2$-de$NO_x$ performance of 0.3Pt/11W/$ZrO_2$ at 125 °C ($X(NO_x)$ ○, $S(N_2)$ ●). Conditions: $m$ = 1.50 g, $c$(NO) = 500 ppm, $c(H_2)$ = 2000 ppm, $c(O_2)$ = 1.5–18 vol.%, Ar balance, $F$ = 500 ml $min^{-1}$ (STP), S.V. = 22.000 $h^{-1}$, $\beta$ = 1.0 K $min^{-1}$.

effect of $O_2$ is systematically investigated, whereas for simplicity the performance of 0.3Pt/11W/$ZrO_2$ is exemplarily illustrated at 125 °C being representative for the low-temperature range (Fig. 6). It is apparent that the $O_2$ concentration does not drastically affect the low-temperature activity, e.g. de$NO_x$ is about 90% for 1.5 vol.% $O_2$ and ca. 75% for 18 vol.%. Moreover, the $N_2$ selectivity does not change at all. On the contrary, the high-temperature activity declines markedly with growing $O_2$ content being completely suppressed above 12 vol.% $O_2$ (Fig. 7). This effect is referred to the increasing reaction of $H_2$ with $O_2$ (Section 3.4). However, diesel engines provide low temperatures in connection with rather high $O_2$ concentrations and vice versa, e.g. at 150 °C the $O_2$ content is in the range of 10–15 vol.%. Therefore, the decline in high-temperature de$NO_x$ observed for relatively high $O_2$ contents is not a substantial issue for practical application.

Furthermore, the effect of CO on $H_2$-de$NO_x$ is investigated as well, since this component is known to block active Pt sites at low temperatures which might affect the performance of 0.3Pt/11W/$ZrO_2$ [27]. For this examination two representative CO concentrations are supplied, i.e. a rather low (40 ppm) and a rather high one (400 ppm). Fig. 8 shows that the latter CO concentration causes

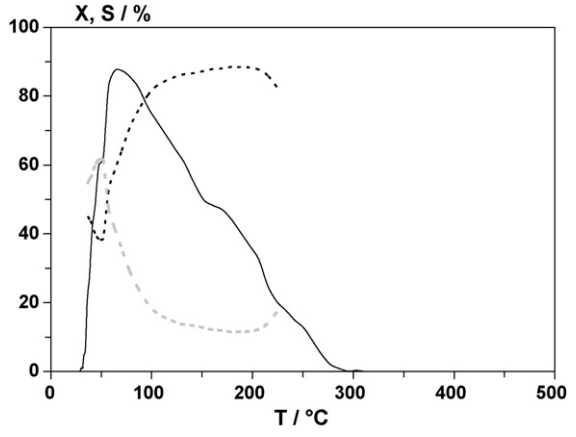


**Fig. 7.** $H_2$-de$NO_x$ performance of 0.3Pt/11W/$ZrO_2$ with a $O_2$ content of 12 vol.% ($X(NO_x)$ —, $S(N_2)$ - -, $S(N_2O)$ ▬ ▬). Conditions: $m$ = 1.50 g, c(NO) = 500 ppm, $c(H_2)$ = 2000 ppm, $c(O_2)$ = 12 vol.%, Ar balance, $F$ = 500 ml $min^{-1}$ (STP), S.V. = 22.000 $h^{-1}$, $\beta$ = 1.0 K $min^{-1}$.

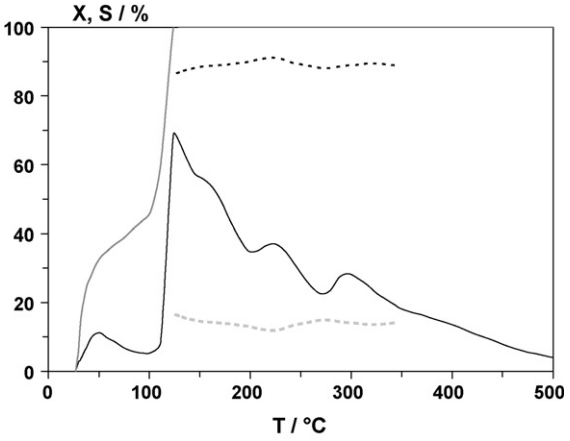


**Fig. 8.** Effect of CO on the $H_2$-deNO$_x$ performance of 0.3Pt/11W/$ZrO_2$ ($X$(NO$_x$) —, $S$($N_2$) - -, $S$($N_2O$) ▬ ▬, $X$(CO) —). Conditions: $m$ = 1.50 g, $c$(NO) = 500 ppm, $c$(CO) = 400 ppm, $c$($H_2$) = 2000 ppm, $c$($O_2$) = 6.0 vol.%, Ar balance, $F$ = 500 ml min$^{-1}$ (STP), S.V. = 22.000 h$^{-1}$, $\beta$ = 1.0 K min$^{-1}$.

a drastic decline in catalytic activity, whereupon significant deNO$_x$ begins in parallel to the CO light-off (ca. 110 °C). This effect is in line with the literature which shows the appearance of free Pt sites being capable of reducing NO only when CO removal starts [29]. Consequently, as deNO$_x$ is inhibited below 110 °C no substantial quantity of $N_2O$ is formed resulting in an overall $N_2$ selectivity of about 90%. Additionally, it is worth mentioning that four maxima of NO$_x$ conversion appear pointing to a broad variety of active Pt sites. Furthermore, the CO concentration of 40 ppm does not affect the performance of 0.3Pt/11W/$ZrO_2$ at all. These results clearly show that high CO concentrations have to be avoided in practice to maintain $H_2$-deNO$_x$. Indeed, this can be simply achieved by using a diesel oxidation catalyst (DOC) located in front the $H_2$-deNO$_x$ catalyst. DOC systems are a state-of-the-art technology and are applied in every diesel vehicle released in the industry countries oxidising CO and HC close to the engine outlet.

### 3.3.2. Hydrothermal stability and resistance against $SO_x$

For the use of 0.3Pt/11W/$ZrO_2$ in diesel exhaust its hydrothermal resistance as well as chemical stability towards $SO_x$ is of particular concern. To pursue these requirements the catalyst (1.50 g) is hydrothermally aged at 780 °C for 15 h adjusting a gas mixture of 2.5 vol.% $H_2O$ and 97.5 vol.% Ar (500 ml/min, STP), whereas exposure to $SO_x$ is carried out at 350 °C for 24 h while supplying a blend of 40 ppm $SO_2$ and synthetic air (500 ml min$^{-1}$, STP). The latter conditions are considered to be appropriate to form $SO_3$ on the catalyst being a strong catalyst poison [30]. Nevertheless, both aging procedures do not affect the catalytic performance at all evidencing high resistance of 0.3Pt/11W/$ZrO_2$ against hydrothermal and sulphur exposure.

### 3.3.3. Comparison of the reducing efficiency of $H_2$ with $C_3H_6$ and CO

To assess the efficiency of $H_2$ in the deNO$_x$ reaction on 0.3Pt/11W/$ZrO_2$ additional reductants are used. For this purpose $C_3H_6$ and CO are taken as they are potentially formed as major or side product in the on-board production of $H_2$ from diesel, e.g. by catalytic cracking, catalytic partial oxidation or catalytic steam reforming [31]; $C_3H_6$ is taken as a model hydrocarbon. For an accurate comparison 10,000 ppm $H_2$, 1000 ppm $C_3H_6$ or 9000 ppm CO are dosed to the standard feed. These concentrations demand very similar amount of oxygen for complete conversion. Fig. 9 shows that the presence of 10,000 ppm $H_2$ causes outstanding NO$_x$ conversion. Contrary, in the study with

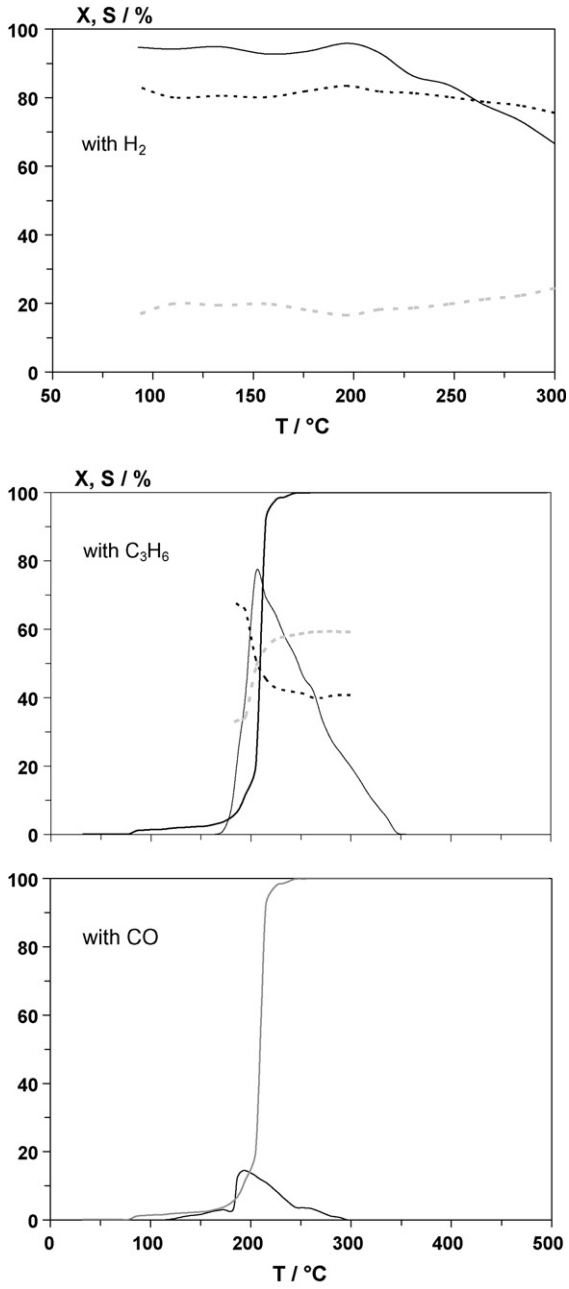


**Fig. 9.** Effect of $H_2$, $C_3H_6$ and CO on the deNO$_x$ performance of 0.3Pt/11W/$ZrO_2$ ($X$(NO$_x$) —, $S$($N_2$) - -, $S$($N_2O$) ▬ ▬, $X$($C_3H_6$) —, $X$(CO) —), The concentration of reducing agent 10,000 ppm $H_2$, 1000 ppm $C_3H_6$ or 9000 ppm CO; remaining conditions are the same as described in Fig. 5.

$C_3H_6$ significant deNO$_x$ appears between 160 and 320 °C only with a peak conversion of ca. 80% corresponding to a $N_2$ selectivity of 45%. A minor deNO$_x$ activity is obtained with CO being in line with the results demonstrated in Section 3.3.1. As discussed there, the inhibition of deNO$_x$ is related to the blocking of active Pt sites by $C_3H_6$ and CO suppressing substantial dissociation of NO [29]. This effect is obviously stronger for CO, whereas it has to be taken into account that much more CO molecules are dosed as compared to $C_3H_6$. Additionally, Fig. 9 demonstrates that $C_3H_6$ and CO mainly react with $O_2$, particularly above 300 °C. Finally, from the present experiments it is concluded that among the tested reductants only $H_2$ shows efficient NO$_x$ reduction on 0.3Pt/11W/$ZrO_2$.

**Table 2**
Model feeds used in the evaluation of the coated honeycomb system[a,b]

| | Simulated raw exhaust | Exhaust with simulated pre-catalyst (DOC) |
|---|---|---|
| $c(NO)$ (ppm) | 500 | 500 |
| $c(H_2)$ (ppm) | 5000 | 5000 |
| $c(CO)$ (ppm) | 500 | 0 |
| $c(C_3H_6)$ (ppm) | 500 | 0 |
| $c(O_2)$ (vol.%) | 5 | 5 |
| $c(H_2O)$ (vol.%) | 10 | 10 |
| $c(CO_2)$ (vol.%) | 10 | 10 |
| $c(N_2)$ | Balance | Balance |

[a] $F$ = 10 l/min (STP), S.V. = 70,000 $h^{-1}$.
[b] Load of catalyst: 100 g $l^{-1}$.

### 3.4. Transfer to honeycomb system

To evaluate the technical potential of 0.3Pt/11W/$ZrO_2$ a full size cordierite monolith (cell density: 400 cpsi) is coated with the catalyst. The impregnation is made by Umicore (Hanau). The catalyst load is established to be 100 g $l^{-1}$ being typically applied for TWC systems. For the catalytic studies a cylindrical core ($d$ = 20 mm, $l$ = 27 mm) is separated from the monolith. The measurements are performed on the same laboratory bench as described in Section 2.4 using a quartz glass tube reactor (i.d. 21 mm) and adjusting a total flow of 10 l $min^{-1}$ (STP). The flow corresponds to a space velocity of 70,000 $h^{-1}$ being representative for high partial load conditions of diesel passenger cars. As the feed is balanced by $N_2$, the selectivity of $N_2$ is calculated from the mass balance based on the traces of $NO_x$ and $N_2O$ (Eqs. (2) and (3)); catalytic data are recorded under stationary conditions.

The catalyst is evaluated by employing two model feeds (Table 2). The first one simulates a raw exhaust using again $C_3H_6$ as model HC. The second feed represents a composition arising from the use of a pre-catalyst (DOC) oxidising CO and HC completely. In both feeds the content of $H_2$ is 5000 ppm, whereas soot is not considered. However, modern diesel vehicles exhibit a DOC coupled with a wall flow filter system (DPF) removing quantitatively particulate matter as well. Thus, the latter model exhaust is closer to practice.

Fig. 10 shows negligible activity of the coated honeycomb in the simulated raw exhaust. This is in agreement with Sections 3.3.1 and 3.3.3 demonstrating that $C_3H_6$ and CO cover the active Pt surface thus inhibiting deNO$_x$; a slight $NO_x$ conversion

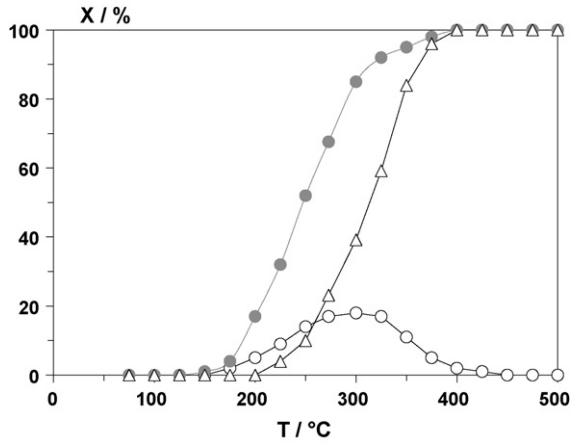


**Fig. 10.** $H_2$-deNO$_x$ performance of honeycomb supported 0.3Pt/11W/$ZrO_2$ in a diesel model raw exhaust ($X(NO_x)$ ○, $X$(CO) ●, $X(C_3H_6)$ △). Conditions are listed in Table 2.

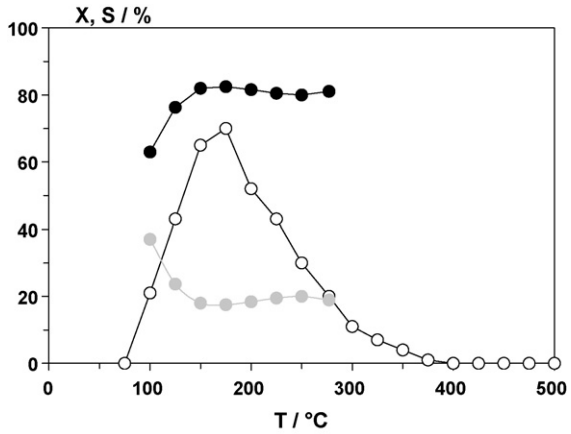


**Fig. 11.** $H_2$-deNO$_x$ performance of honeycomb supported 0.3Pt/11W/$ZrO_2$ in a diesel model exhaust simulating use of a DOC pre-catalyst ($X(NO_x)$ ○, $S(N_2)$ ●, $S(N_2O)$ ●). Conditions are listed in Table 2.

appears only when the HC and CO oxidation starts resulting in 20% deNO$_x$ at 300 °C. However, at these temperatures $H_2$ mainly reacts with the excessive $O_2$ thus declining deNO$_x$. This again evidences the need of a DOC for the use of 0.3Pt/11W/$ZrO_2$ in practice. Hence, it is not surprising that in the absence of HC and CO the catalyst reveals pronounced low-temperature performance (Fig. 11). When the other feed is dosed simulating the presence of a pre-catalyst (DOC) peak $NO_x$ conversion is 60% appearing at 150 °C, while $S(N_2)_{overall}$ is found to be 80%. Furthermore, these features clearly show that the $H_2$-deNO$_x$ profile is similar to the powder sample thus proving satisfactory transfer to the honeycomb system. However, as compared to the powder experiments (Fig. 5) the $NO_x$ conversion below 100 °C is less being referred to the higher space velocity and the presence of water partially covering active sites [27,29].

For the examination of the effect of $H_2$ on the low-temperature performance of 0.3Pt/11/$ZrO_2$ the hydrogen concentration is systematically varied from 2000 to 10,000 ppm. In these investigations the model exhaust is used assuming a DOC pre-catalyst. The measurements are made at 150 °C as Fig. 11 shows peak deNO$_x$ activity at this temperature. The results of $H_2$ variation point to rather limited influence of the reducing agent (Fig. 12). The $NO_x$ conversion slightly increases when the concentration grows from 2000 to 5000 ppm; higher contents do not provide any increase in deNO$_x$. The latter feature seems to be surprising as increasing concentration of $H_2$ is expected to cause higher $NO_x$ conversion. However, it has to be taken into account that the total flow of 10 l $min^{-1}$ includes a substantial supply of $H_2$, e.g. for 5000 ppm it is 50 ml $min^{-1}$. This specific flow causes a drastic heat production particularly for $H_2$ contents above 6000 ppm resulting in outlet temperatures being ca. 60 K above the inlet. As a consequence, the temperature of the catalyst exceeds its optimum operation window. Based on these results it is apparent that for the present honeycomb prototype the optimum $H_2$ concentration is about 5000 ppm. Additionally, the $H_2$ concentration reveals minor effect on the $N_2$ selectivity as deduced from Fig. 12 as well.

Furthermore, Fig. 12 also displays the selectivity of $H_2$ for deNO$_x$ ($S(H_2)$); $S(H_2)$ represents the fraction of reducing agent being involved in deNO$_x$. It is assumed that for the reduction of one NO molecule, that is exclusively dosed, one $H_2$ is required to form $N_2$ (Eq. (5)), while for the production of $N_2O$ it is half amount of $H_2$ (Eq. (6)). Additionally, a GC/TCD analysis (GC14B, Shimadzu) of $H_2$-deNO$_x$ on 0.3Pt/11W/$ZrO_2$ indicates complete $H_2$ consumption above 100 °C. Thus, the deNO$_x$ selectivity of $H_2$ is estimated by

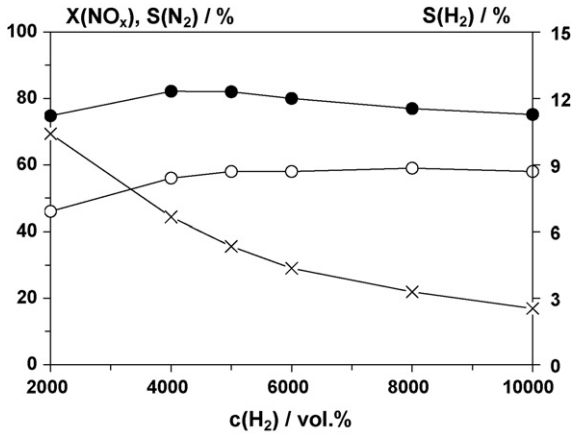


**Fig. 12.** Effect of $H_2$ on deNO$_x$ performance and $H_2$ selectivity of honeycomb supported 0.3Pt/11W/$ZrO_2$ in a diesel model exhaust simulating use of a DOC pre-catalyst ($X$(NO$_x$) ○, $S$($N_2$) ●, $S$($H_2$) ×). Conditions are listed in Table 2, while the $H_2$ concentration is varied from 2000 to 10,000 ppm; $T_{inlet}$ = 150 °C.

Eq. (7) using the experimental traces of NO$_x$ and $N_2O$.

$$2NO + 2H_2 \rightarrow N_2 + 2H_2O \quad (5)$$

$$2NO + H_2 \rightarrow N_2O + H_2O \quad (6)$$

$$S(H_2) = \frac{c(NO_x)_{in} - c(NO_x)_{out} - c(N_2O)}{c(H_2)_{in}} \quad (7)$$

Fig. 12 demonstrates a very low selectivity of $H_2$ for deNO$_x$ being less than 10%. This result provides evidence that the conversion of $H_2$ with excessive $O_2$ represents the major reaction, whereas deNO$_x$ is just a side reaction. Hence, in respect of the reducing agent $H_2$-deNO$_x$ performed under lean conditions has to be defined as a non-selective reaction being reflected by minor efficiency of $H_2$.

### 3.5. Mechanistic aspects of $H_2$-deNO$_x$

#### 3.5.1. DRIFTS study using the probe molecule CO

The DRIFT spectra of 0.5Pt/$Al_2O_3$, 0.3Pt/$ZrO_2$ and 0.3Pt/11W/$ZrO_2$ recorded after exposure to the probe molecule CO reveal a prominent band ranging from ca. 2000 to approximately 2100 cm$^{-1}$ (Fig. 13) This absorption is attributed to the stretching

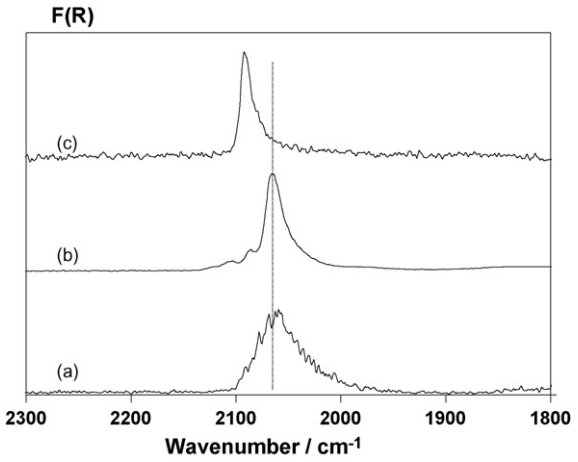


**Fig. 13.** DRIFT spectra of 0.5Pt/$Al_2O_3$ (a), 0.3Pt/$ZrO_2$ (b) and 0.3Pt/11W/$ZrO_2$ (c) after CO exposure at 25 °C.

vibration of CO linearly bonded to Pt sites, whereas no signal appears at about 1850 cm$^{-1}$ which might be assigned to CO bridging two Pt sites [32,33]. Additionally, the DRIFTS band of 0.5Pt/$Al_2O_3$ is relatively broad, while 0.3Pt/$ZrO_2$ shows two high frequency shoulders. These features are referred to CO adsorbed on different Pt sites as reported in the literature [34]. Moreover, the peak of the latter is located at a slightly higher frequency as compared to 0.5Pt/$Al_2O_3$, whereas the signal of 0.3Pt/11W/$ZrO_2$ reveals a clearer shift of ca. 30 cm$^{-1}$. This effect is interpreted with electronic interactions of the $WO_3$ component and Pt. It is assumed that the promoter transfers electrons to the precious metal hence increasing the electron density on the Pt. Consequently, the (Pt–C) bond weakens, whereby the (C–O) bond is strengthened resulting in a higher vibration frequency as compared to the corresponding Pt/$ZrO_2$ and Pt/$Al_2O_3$ systems. However, it should be stated that the $\nu$(CO) band of gaseous CO appears at ca. 2145 cm$^{-1}$ showing weaker (C–O) bond strength of adsorbed CO, even for 0.3Pt/11W/$ZrO_2$. Finally, very similar DRIFT spectra are obtained for the samples revealing a Pt content of 2 wt.% (vide infra).

#### 3.5.2. Kinetic modelling of $O_2$-TPD

For confirmation of the electronic interactions between promoter and Pt TPD studies are performed using $O_2$ as probe molecule ($O_2$-TPD). The $O_2$ desorption profiles are numerically modelled to obtain the activation energy of $O_2$ release as well as the Pt coverage by oxygen. In the $O_2$-TPD examinations Pt loads of 2 wt.% are taken as no significant desorption signals appear with lower contents. These model catalysts, i.e. 2Pt/$Al_2O_3$, 2Pt/$ZrO_2$ and 2Pt/11W/$ZrO_2$, show very similar order in $H_2$-deNO$_x$ performance. The $O_2$-TPD spectra are depicted in Fig. 14, whereas the profiles are quite akin exhibiting a broad desorption signal with a shoulder at higher temperature. In the kinetic model the $O_2$ adsorption/desorption equilibrium is described by Eq. (8) assuming dissociative adsorption of $O_2$ on the active Pt sites (*) being in accordance with the literature [27]. The present approach represents a mean field model considering the different types of Pt sites to be equivalent. This approximation is generally applied for the kinetic modelling of gas/solid systems as stated in Ref. [35].

$$O_{2(g)} + 2* \underset{r_2}{\overset{r_1}{\rightleftarrows}} 2O* \quad (8)$$

For the adsorption and desorption an Arrhenius-based rate expression is defined in (Eqs. (9) and (10)); $A_1$ and $A_2$ are the corresponding pre-exponential factors, $E_1$ the activation energy of adsorption, $E_2(0)$ the activation energy of desorption at zero coverage, $\theta_O$ the oxygen coverage and $\theta_*$ the number of free Pt sites. The repulsion of surface oxygen species is supposed to linearly decrease the activation energy of desorption with increasing coverage; for this purpose the constant $\alpha$ is introduced [27].

$$r_1 = A_1 \exp\left(-\frac{E_1}{RT}\right) c_{O_2(g)} \theta_*^2 \quad (9)$$

$$r_2 = A_2 \exp\left(-\frac{E_2(0) - \alpha\theta_O}{RT}\right) \theta_O^2 \quad (10)$$

Moreover, the kinetic model is based upon the mass balance of the gaseous (Eq. (11)) and adsorbed oxygen species (Eq. (12)); $F$ is the flow, $A_{cat}$ the active surface of Pt, $\Gamma_{cat}$ the surface concentration of the active Pt sites and $\nu_j$ the stoichiometric coefficient.

$$Fc(O_2)_{in} - Fc(O_2)_{out} + A_{cat} \sum_j^{N_j} \nu_j r_j = 0 \quad (11)$$

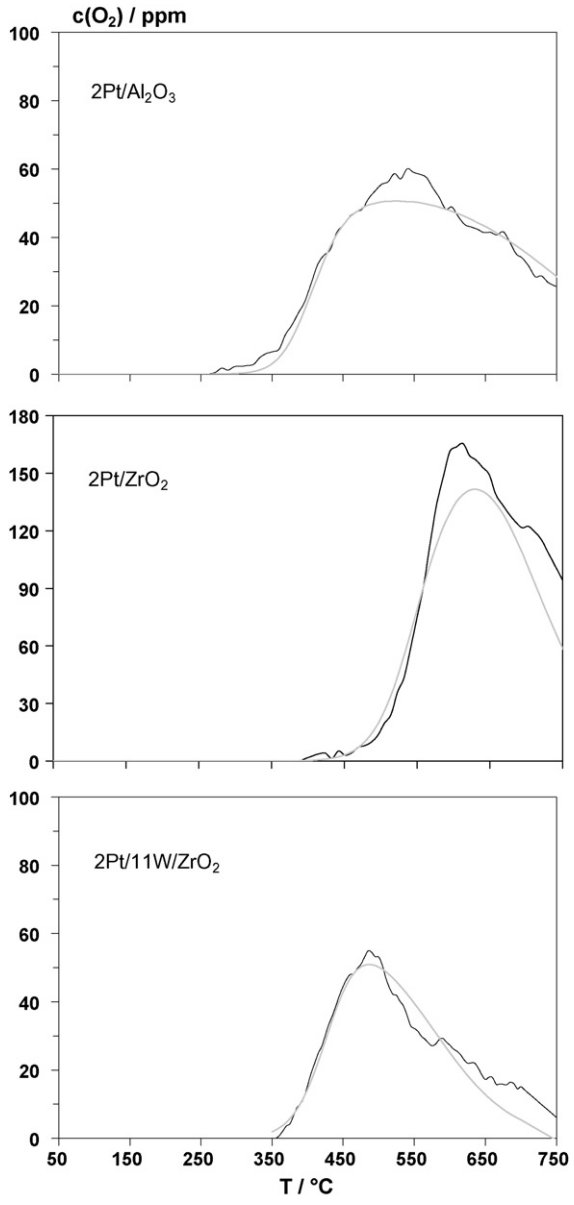


**Fig. 14.** Experimental (–) and fitted $O_2$-TPD patterns (▬) of $2Pt/Al_2O_3$, $2Pt/ZrO_2$ and $2Pt/11W/ZrO_2$. Conditions: $m$ = 5.00 g, $F$ = 500 ml min$^{-1}$ (STP), $\beta$ = 20 K min$^{-1}$.

$$A_{act}\Gamma_{act}\beta\frac{d\theta}{dT} = A_{act}\sum_{j}^{N_j}\nu_j r_j \tag{12}$$

The mass balance of gas-phase and adsorbed oxygen results in a system of one algebraic (Eq. (13)) and one non-linear differential equation (Eq. (14)).

$$c(O_2)_{out} = \frac{A_{act}A_2\exp(-E_2(0)(1-\alpha\theta_O)/RT)\theta_O^2}{F + A_{act}A_1\exp(-E_1/RT)(1-\theta_0)^2} \tag{13}$$

$$A_{act}\Gamma_{cat}\beta\frac{d\theta}{dT} = 2A_{act}A_1\exp\left(-\frac{E_1}{RT}\right)c(O_2)_{out}(1-\theta_0)^2 - 2A_{act}A_2\exp\left(-\frac{E_2(0)(1-\alpha\theta_O)}{RT}\right)\theta_O^2 \tag{14}$$

It should be stated that Eq. (11) describes the used plug flow reactor by the model of continuously stirred tank reactor, i.e. the differential term of the former is neglected assuming stationary conditions. This approach has been reported to be a fair approximation in TPD modelling [35]. The surface coverage and free parameters are calculated by using the Matlab tools ode 15 s and Isqcurvefit.

The active surface area ($A_{act}$) is simply calculated from the load of Pt, $d_{Pt}$, $n_{H_2}$, the $H_2$/Pt adsorption stoichiometry (Eq. (1)) and the surface area per Pt site ($a_m = 8.02 \times 10^{-20}$ m$^2$ site$^{-1}$ [25]) leading to 2.2, 4.0 and 2.6 m$^2$ for $2Pt/Al_2O_3$, $2Pt/ZrO_2$ and $2Pt/W/ZrO_2$, respectively.

To decrease the number of free parameters in the fit procedure the pre-exponential factor for the $O_2$ desorption ($2 \times 10^{10}$ mol s$^{-1}$ m$^{-2}$) is taken from the literature [36]. Additionally, the $O_2$ adsorption is assumed not to be activated being in good correspondence with literature, i.e. $E_1$ = 0 kJ mol$^{-1}$ [29,37]. Furthermore, the pre-exponential factor of the adsorption is calculated by using the kinetic gas theory [38,39], whereupon the sticking coefficient at zero coverage ($S^0$ = 0.07 [38]) and $\Gamma_{cat}$ (0.26 μmol m$^{-2}$ [27]) are adopted from literature. In the calculation the temperature dependency is neglected by using an average temperature of $O_2$-TPD, i.e. 350 °C. Hereby, $A_1$ is determined to be 8.1 m s$^{-1}$.

$$A_1 = \frac{N_A RT}{(2\pi M_i RT)^{0.5}} a_m \Gamma_{cat} S^0 \tag{15}$$

In the numeric modelling of $O_2$-TPD $A_1$, $E_1$ and $A_2$ are kept fixed, while $\theta_O$, $E_2(0)$ and $\alpha$ are fitted. The results of the calculations are presented in Fig. 14 showing a satisfactory description of the experimental traces by the kinetic parameters implemented in the model. The estimated parameters are demonstrated in Table 3 along with the 95% confidence interval indicating high reliability of the calculations. The comparison of $E_2(0)$ of $2Pt/Al_2O_3$ with literature shows good agreement with results from a Pt(1 1 1) single crystal surface providing 213 kJ mol$^{-1}$ [40]; values of 200 kJ/mol are reported on polycrystalline Pt being close to the data of $2Pt/Al_2O_3$ and $2Pt/ZrO_2$. Additionally, the features for $\alpha$ are typical for polycrystalline Pt as well [27,38,41].

Furthermore, Table 3 demonstrates that the activation energy for $O_2$ desorption declines in the sequence $2Pt/Al_2O_3 > 2Pt/ZrO_2 > 2Pt/11W/ZrO_2$. Taking this activation energy as a measure for the strength of the (Pt–O) bond it is deduced that $Pt/Al_2O_3$ reveals the strongest and $2Pt/11W/ZrO_2$ the weakest bonding. This result is in line with the DRIFTS examinations taking CO as probe molecule. As a consequence, the calculated activation energies of $O_2$ desorption substantiate the electronic interaction of Pt and $WO_3$. Moreover, the oxygen coverage obtained from the numerical modelling as well shows the same order as $E_2(0)$, i.e. $2Pt/Al_2O_3$ exhibits the highest and $2Pt/11W/ZrO_2$ the lowest initial coverage (Table 3). Based on the above interpretation it is apparent that the increased electron density on Pt leads to declining adsorption of $O_2$ corresponding to a higher fraction of free Pt sites. Transferring this feature to $H_2$-de$NO_x$ it may be derived that an increased quantity of available Pt sites directly enhances the catalytic activity. Additionally, Burch indicates that a larger abundance of Pt sites favours the probability of $N_2$ formation; for the production of $N_2$ four neighbouring sites are required, while for $N_2O$ it is three only [2].

**Table 3**
Kinetic parameters of the adsorption/desorption of $O_2$ on $2Pt/Al_2O_3$, $2Pt/ZrO_2$ and $2Pt/11W/ZrO_2$ including the 95% confidence interval

| Parameter | $2Pt/Al_2O_3$ | $2Pt/ZrO_2$ | $2Pt/11W/ZrO_2$ |
|---|---|---|---|
| $\theta_O$[a] (%) | 82 | 73 | 38 |
| $E_2(0)$ (kJ mol$^{-1}$) | 217 ± 1 | 196 ± 2 | 172 ± 1 |
| $\alpha$ (kJ mol$^{-1}$) | 0.23 ± 0.01 | 0.01 ± 0.002 | 0.24 ± 0.03 |

[a] Initial Pt coverage by oxygen.

Thus, it is likely that a rising number of free Pt sites increases the catalytic activity as well as $N_2$ selectivity. Furthermore, according to Burch a weaker (Pt–O) binding energy should enhance the regeneration of the active Pt sites by $H_2$ supporting the performance as well. Consequently, by combining the present results with the mechanism from Burch a fair explanation of the specific $H_2$-de$NO_x$ performance of $Pt/Al_2O_3$, $Pt/ZrO_2$ and $Pt/W/ZrO_2$ is provided. Finally, without considering the discussed electronic interactions the use of the dispersion of Pt (Table 1) is not feasible for the interpretation of the $H_2$-de$NO_x$ data of the different catalytic systems.

### 3.5.3. DRIFTS study of the $H_2$-de$NO_x$ reaction

The mechanism of the $H_2$-de$NO_x$ reaction is investigated by DRIFT spectroscopy using the $2Pt/11W/ZrO_2$ model catalyst and the $2Pt/ZrO_2$ reference again; for the samples with Pt contents of 0.3 wt.% NO species on Pt are not detectable as deduced from preliminary studies. Fig. 15 displays the DRIFTS data of $2Pt/ZrO_2$ showing that exposure to $NO/O_2$ results in strong bands at 1580 and 1615 $cm^{-1}$ with a shoulder at about 1560 $cm^{-1}$. Additionally, weak signals appear at 1235, 1720, 1790 and 1860 $cm^{-1}$. The peaks below 1650 $cm^{-1}$ are observed for pure $ZrO_2$ as well and are therefore assigned to $NO_x$ species present on the support. The 1235 $cm^{-1}$ feature is referred to nitrite ($\nu_{as}(NO_2)$), while the signals at 1580 and 1615 $cm^{-1}$ are assigned to nitrato species coordinated to $Zr^{4+}$ Lewis acid sites [32,42]; the formation of $NO_2^-$ and $NO_3^-$ species is best known for metal oxides reacting with $NO_x$. Additionally, the shoulder at 1560 $cm^{-1}$ indicates the presence of different types of nitrato species like unidentate, bidentate and bridging entities, whereas an unequivocal assignment is difficult due to same symmetry ($C_{2v}$). Furthermore, the weak DRIFTS bands located at 1720, 1790 and 1860 $cm^{-1}$ are associated with the stretching vibration of NO linearly coordinating to Pt particles of different sizes [27,43]. However, we do not exclude NO coordinated to different Pt sites, e.g. steps and kinks. Fig. 15 shows that the bands of the Pt–NO species decrease when adding the mixture of 40 ppm $H_2$ and 6 vol.% $O_2$. In contrast to that, the $NO_x$ species adsorbed on the support are not affected, i.e. the nitrato peaks rather increase slightly as the support surface is apparently not saturated taking up $NO_x$ desorbing from the stainless steel pipes. The same effects are observed for the mixture of 2000 ppm $H_2$ and 6 vol.% $O_2$.These results provide evidence that $H_2$-de$NO_x$ on $Pt/ZrO_2$ follows the mechanism from Burch including NO reduction on the Pt component only. Hence, the route from Costa is excluded implying considerable participation of $NO_x$ species being present on the support as demonstrated for $Pt/La_{0.7}Sr_{0.2}Ce_{0.1}FeO_3$ [12] and $Pt/MgO–CeO_2$ [13]. Finally, no substantial change in the spectral range above 2700 $cm^{-1}$ is observed indicating that $H_2O$ originated from $H_2$ oxidation is hardly adsorbed on the catalyst (inset of Fig. 15).

The DRIFTS study of $2Pt/11W/ZrO_2$ follows the same experimental procedure as for $Pt/ZrO_2$, whereas it has to be mentioned that the reflectance of the former catalyst is much lower being related to the strong absorption of tungsten oxide. As a consequence, the spectra exhibit a significantly diminished $S/R$ ratio, whereby in the $NO/O_2$ exposure an unresolved signal of Pt–NO species ($\nu$(NO) at ca. 1800 $cm^{-1}$) is observed only (Fig. 16). Moreover, the data obtained from $NO_x$ treatment imply very similar features below 1700 $cm^{-1}$ as for $Pt/ZrO_2$ thus being interpreted with nitrite and nitrate species adsorbed on the carrier. This assignment is also confirmed by a blank experiment exposing $11WO_3/ZrO_2$ to the $NO/O_2$ mixture. In this experiment additional signals are observed from 2050 to 2200 $cm^{-1}$ arising for $2Pt/11WO_3/ZrO_2$ as well (Fig. 16); in Fig. 16 the spike at ca. 2020 $cm^{-1}$ represents an artefact. As derived from literature the features be ascribed to $NO^+$, $NO_2^+$, $(NO)^{\delta+}$ or $(NO_2)^{\delta+}$ species [32,42,43]. It is obvious that these entities are exclusively coordinated to the $WO_3$ component, most likely to Lewis acid $W^{6+}$ sites. Furthermore, these species are not assumed to be involved in $H_2$-de$NO_x$; indeed their bands decrease upon dosage of $H_2/O_2$, but the same decline with time is also observed in Ar flow indicating reversible adsorption. Contrary, reaction with $H_2$ is clearly observed for the Pt–NO species, whereas even after a reaction time of 12 min a significant feature remains. Moreover, the nitrato species increase slightly in the beginning of $H_2$ exposure being associated with $NO_x$ desorption from the stainless steel bench as discussed above for $Pt/ZrO_2$. However, in contrast to the reference, the 1620 $cm^{-1}$ band grows drastically and shifts to 1610 $cm^{-1}$ with reaction time. In parallel to that, a broad signal appears in the OH stretching vibration range (inset of Fig. 16). Thus, the increasing bands at 1610 and ca. 3500 $cm^{-1}$ are assigned to the adsorption of $H_2O$ formed in $H_2$ oxidation. As this effect is not observed for $Pt/ZrO_2$ it is concluded that the water is mainly adsorbed on $WO_3$. However, the intensity of the 1610 $cm^{-1}$ band ($\delta(H_2O)$) is usually much weaker than the

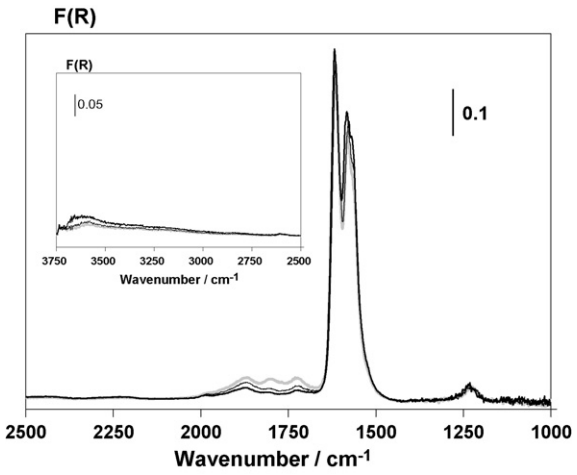


**Fig. 15.** DRIFT spectra of $2Pt/ZrO_2$ recorded at 125 °C after exposure to 1000 ppm NO and 6 vol.% $O_2$ and subsequent purging with Ar (—) followed by supplying 40 ppm $H_2$ and 6 vol.% $O_2$ for 1 min (–) and 10 min (–). The inset shows the corresponding OH stretching region.

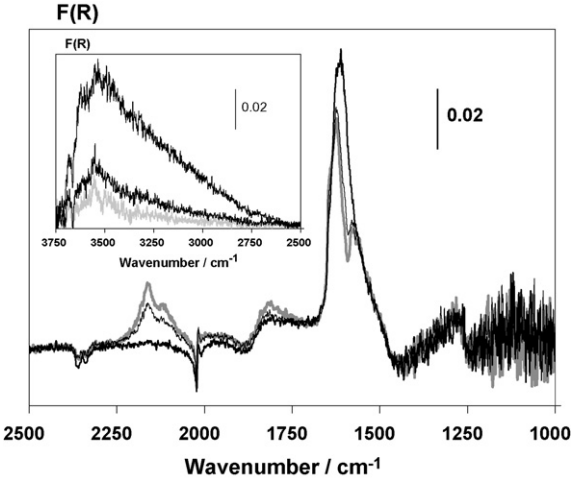


**Fig. 16.** DRIFT spectra of $2Pt/11W/ZrO_2$ recorded at 125 °C after exposure to 1000 ppm NO and 6 vol.% $O_2$ and subsequent purging with Ar (—) followed by supplying 40 ppm $H_2$ and 6 vol.% $O_2$ for 1 min (–) and 12 min (–). The inset shows the corresponding OH stretching region.

feature of the OH stretching vibration, whereas a rough estimation provides a ratio of about 3. In fact, by adopting this ratio and adding the resulting intensity of $\delta(H_2O)$ to the initial nitrato peak the recorded feature at 1610 $cm^{-1}$ is quantified well. This estimation indicates that the nitrato species remain on the catalyst in substantial amount during $H_2/O_2$ exposure. A very similar conclusion is drawn for the nitrite species not being affected at all by the supply of $H_2$ (Fig. 16).

Summarising these results it is supposed that the $NO_x$ species adsorbed on the support are not involved in $H_2$-de$NO_x$ on 2Pt/11W/$ZrO_2$ as well as Pt/$ZrO_2$. In contrast to that, complete disappearance of the $NO_x$ surface species is obtained by treating $11WO_3/ZrO_2$ with a mixture of $H_2/N_2$ (125 °C). This indicates that in principle the reaction of nitrite and nitrate entities with $H_2$ is possible, but is entirely suppressed in presence of Pt and excessive $O_2$; obviously, the conversion of $H_2$ with oxidised Pt sites is much faster then.

Furthermore, in another blank DRIFTS experiment 2Pt/11W/$ZrO_2$ is exposed to $H_2O$ typically leading to the band at 1610 $cm^{-1}$ and the broad feature above 2500 $cm^{-1}$, while a rather broad signal is additionally observed at 1740 $cm^{-1}$. This unexpected band might explain the peak in the range of the $\nu$(NO) vibration (Pt-NO) remaining during $H_2/O_2$ treatment (Fig. 16). Nevertheless, the accurate assignment of the band is difficult; it may be speculated that it is related to $H_2O$ adsorbed on specific sites of the $WO_3$ promoter. Moreover, it is worth mentioning that, in contrast to Pt/$ZrO_2$, adsorbed water still exists on the 2Pt/11W/$ZrO_2$ catalyst at 125 °C. This effect is in accordance with literature indicating stabilisation of molecular water on $WO_3/ZrO_2$ systems up to 300 °C [44]. Additionally, another DRIFTS study demonstrates that even after a final purging with Ar for 20 min (125 °C) the 1620 $cm^{-1}$ band is more intense than the initial nitrato peak.

### 3.5.4. $NO_x$-TPD studies

The $NO_x$-TPD studies provide a very similar trend regarding the reactivity of the $NO_x$ surface species as found by DRIFTS. The inset of Fig. 17 demonstrates the TPD pattern of 0.3Pt/11W/$ZrO_2$ corresponding to a $NO_x$ uptake of 12.5 μmol/g. In accordance with the DRIFTS results (Fig. 16) and literature indicating very low Pt coverage by $NO_x$ in $NO/O_2$ exposure [27] we mainly attribute the desorption signal to the decomposition of nitrate species. When $H_2/O_2$ is added after the $NO/O_2$ exposure nitrate species are immediately decomposed as indicated by the prompt desorption of $NO_x$ amounting to 9.0 μmol/g (Fig. 17). This effect may be ascribed to local increase in temperature that is associated with the oxidation of $H_2$, whereas the outlet TC does not monitor a significant heat production being similar to the $H_2$-de$NO_x$ studies (Section 2.4). The following TPD results in a $NO_x$ release of 3.3 μmol/g. The sum of the desorbed amounts of $NO_x$ is close to the quantity determined without intermediate $H_2/O_2$ exposure excluding the contribution of $NO_x$ species of the support in $H_2$-de$NO_x$. The slight difference in the $NO_x$ balance (0.2 μmol/g) as compared to the TPD without $H_2/O_2$ treatment might be assigned to the reduction of $NO_x$ adsorbed and/or readsorbed on the Pt component; however, it has to mentioned that this small amount is in the range of the reproducibility of the TPD runs and therefore a definite interpretation is difficult. A different result is obtained when the $H_2$/Ar mixture is dosed before the start of TPD leading to a $NO_x$ desorption of 1.1 μmol/g only appearing exclusively in TPD. This indicates a substantial $NO_x$ conversion in the $H_2$ treatment (ca. 11.4 μmol/g) being in line with the DRIFTS data obtained after dosage of $H_2$/Ar. Thus, the $NO_x$-TPD investigations substantiate the DRIFTS examinations excluding the participation of the nitrite and nitrate species in $H_2$-de$NO_x$. It should finally be mentioned that SSTIKA (steady-state transient isotopic kinetic analysis) is considered to be a powerful tool as well to study the site location of the active $NO_x$ species [12].

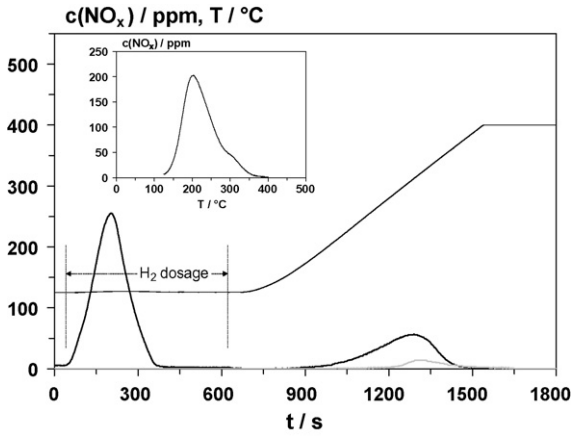


**Fig. 17.** $NO_x$-TPD patterns of 0.3Pt/11W/$ZrO_2$ without $H_2$ exposure (inset) and with intermediate exposure to 1500 ppm $H_2$ and 6 vol.% $O_2$ in Ar (–) and to 1500 ppm $H_2$ in Ar (▬). Conditions: $m$ = 1.50 g, $F$ = 500 ml $min^{-1}$ (STP), $\beta$ = 20 K $min^{-1}$.

## 4. Conclusions

In this paper a novel $H_2$-de$NO_x$ catalyst is presented for the low-temperature $NO_x$ removal from oxygen-rich exhaust gases, e.g. diesel exhaust. Low-temperature de$NO_x$ is a challenging issue as under these conditions the favoured de$NO_x$ procedures, i.e. NSR and SCR, reveal limited efficiency only. The developed pattern consists of tetragonal $ZrO_2$ (carrier), amorphous $WO_3$ (promoter) and Pt (catalytic component). The outstanding low-temperature activity and pronounced $N_2$ selectivity of the 0.3Pt/11W/$ZrO_2$ sample is associated with the electronic interaction of Pt and $WO_3$. The promoter increases the electron density on the Pt thus activating the catalyst. Contrary, $NO_x$ species adsorbed on the $WO_3/ZrO_2$ substrate play no role in $H_2$-de$NO_x$. Furthermore, the material maintains its catalytic performance under realistic conditions and is stable towards hydrothermal and $SO_x$ aging being important for practice. However, the sample does not operate at high temperatures (>300 °C) as $H_2$ then reacts completely on the catalyst with the excessive $O_2$. Hence, for the high-temperature regime another catalyst is required to entirely substitute the SCR and NSR procedure; as indicated in the introduction such a catalytic material might be Pd or perovskites potentially revealing lower $H_2$ oxidation activity. However, this work mainly focuses on the low-temperature range being crucial for the breakthrough of $H_2$-de$NO_x$ technology. Furthermore, $H_2$-de$NO_x$ can also be applied in addition to NSR or SCR resulting in an integrated process covering a broad temperature range. Nevertheless, the present studies show that HC and CO inhibits the performance of 0.3Pt/11W/$ZrO_2$ at low temperatures necessitating a DOC pre-catalyst. Additionally, it has to be taken into account that modern diesel engines reveal a DPF unit for soot removal, whereas the $H_2$-de$NO_x$ catalyst should be placed downstream to the filter to avoid soot and ash deposits. Hence, for the integration of $H_2$-de$NO_x$ in an optimum after treatment system the following sequence is suggested: (1) DOC (HC and CO oxidation), (2) DPF (soot removal), (3) NSR or SCR (de$NO_x$) and (4) $H_2$-de$NO_x$ (low-temperature de$NO_x$). The $H_2$-de$NO_x$ stage is located at tailpipe position as it allows lower operation temperatures as compared to NSR or SCR. Moreover, it is worth mentioning that the hydrogen should be directly dosed in front of the $H_2$-de$NO_x$ catalyst to avoid prior oxidation in the exhaust line.

A serious feature of $H_2$-de$NO_x$ is the low efficiency of $H_2$ preferentially reacting with $O_2$ being present in excess; the de$NO_x$ selectivity of $H_2$ is found to be below 10%. The excessive consumption of $H_2$ might be less problematic when the vehicle is equipped with a gas cylinder; e.g. $H_2$ can be produced from biomass [45]. However, the use of a $H_2$ cylinder could be a critical point due to safety objections. Another possibility is the on-board production of $H_2$ from diesel as mentioned in Section 3.3.3, i.e. by using reforming or partial oxidation. Here, the low de$NO_x$ efficiency of $H_2$ directly leads to an additional consumption of fuel representing a very problematic issue. Nevertheless, it has to be taken into consideration that the dosage of $H_2$ is mainly necessary during the acceleration of the vehicle only. From the supposition of $H_2$ production by reforming of *n*-dodecane occurring with an efficiency of 80% an excessive fuel consumption of about 3% is derived for the MVEG test cycle including a molar $H_2$/$NO_x$ ratio of 4 (*n*-dodecane represents a major diesel component). This estimation shows the additional consumption of diesel to be in an acceptable range. However, in the current debate on energy efficiency and $CO_2$ emission this excessive consumption has to be considered critically. On the other hand, catalytic reforming and partial oxidation of diesel is actually developed to increase the engine efficiency. Thus, this research might offer the possibility to produce $H_2$ for de$NO_x$ without excessive fuel consumption as referred to actual engine efficiencies.

## Acknowledgements

The authors acknowledge thankfully the financial support from research programme of Baden-Württemberg county (BWPLUS) for catalyst development as well as the funds from German Research Foundation (DFG) for mechanistic studies. Special thanks go to Umicore (Hanau) for performing the catalytic coating and to Erna Brettner and Prof. Papp from University of Leipzig for XPS measurements.

## References

[1] J.H. Jones, J.T. Kummer, K. Otto, M. Shelef, E.E. Weaver, Environ. Sci. Technol. 9 (1971) 791.
[2] R. Burch, P.J. Millington, A.P. Walker, Appl. Catal. B 4 (1994) 65.
[3] A. Wildermann, Ph.D. Study, University of Erlangen-Nürnberg, 1994.
[4] E. Frank, H. Oguz, W. Weisweiler, Chem. Eng. Technol. 6 (2003) 679.
[5] A. Ueda, T. Nakao, M. Azuma, T. Kobayashi, Catal. Today 45 (1998) 135.
[6] K. Yokota, M. Fukui, T. Tanaka, Appl. Surf. Sci. 121/122 (1997) 273.
[7] B. Frank, G. Emig, A. Renken, Appl. Catal. B 19 (1998) 45.
[8] B. Frank, R. Lübke, G. Emig, A. Renken, Chem. Eng. Technol. 6 (1998) 498.
[9] N. Macleod, R.M. Lambert, Appl. Catal. B 35 (2002) 269.
[10] N. Macleod, R.M. Lambert, Appl. Catal. B 46 (2003) 483.
[11] C.N. Costa, V.N. Stathopoulos, V.C. Belessi, A.M. Efstathiou, J. Catal. 197 (2001) 350.
[12] C.N. Costa, P.G. Savva, C. Andronikou, P.S. Lambrou, K. Polychronopoulou, V.C. Belessi, V.N. Stathopoulos, P.J. Pomonis, A.M. Efstathiou, J. Catal. 209 (2002) 456.
[13] C.N. Costa, A.M. Efstathiou, J. Phys. Chem. C 111 (2007) 3010.
[14] C.N. Costas, P.G. Savva, J.L. Fierro, A.M. Efstathiou, Appl. Catal. B 75 (2007) 147.
[15] J.P. Breen, R. Burch, J. Hardacre, C.J. Hill, B. Krutzsch, B. Bandl-Konrad, E. Jobson, L. Cider, P.G. Blakeman, L.J. Peace, M.V. Twigg, M. Preis, M. Gottschling, Appl. Catal. B 70 (2007) 36.
[16] R.J.H. Voorhoeve, J.P. Remeika, L.E. Trimble, A.S. Cooper, F.J. Disalvo, P.K. Gallagher, J. Solid-state Chem. 14 (1975) 395.
[17] A. Lindsted, D. Strömberg, M.A. Milh, Appl. Catal. A 116 (1994) 109.
[18] D. Ferri, L. Forni, M.A.P. Dekkers, B.E. Nieuwenhuys, Appl. Catal. B 16 (1998) 339.
[19] G.L. Chiarello, D. Ferri, J.-D. Grunwaldt, L. Forni, A. Baiker, J. Catal. 252 (2007) 137.
[20] F.J.P. Schott, Diploma Thesis, University of Karlsruhe, 2003.
[21] J. Adler, Diploma Thesis, University of Karlsruhe, 2006.
[22] F.J.P. Schott, S. Kureti, Report of the BWPLUS project BWI 23002, http://bwplus.fzk.de/inhalt_berichte_bwplusreihe.html.
[23] D. Ciuparu, A. Ensuque, G. Shafeev, F. Bozon-Verduraz, J. Mater. Sci. Lett. 19 (2000) 931.
[24] N. Apostolescu, B. Geiger, K. Hizbullah, M.T. Jan, S. Kureti, D. Reichert, F. Schott, W. Weisweiler, Appl. Catal. B 62 (2006) 104.
[25] G. Bergeret, P. Gallezot, Handbook of Heterogeneous Catalysis, vol. 4, John Wiley, New York, 1997.
[26] D. Briggs, M.P. Seah, Practical Surface Analysis, vol. I, John Wiley, Chichester, 1990
[27] M. Crocoll, S. Kureti, W. Weisweiler, J. Catal. 229 (2005) 480.
[28] D.E. Mears, Ind. Eng. Chem. Process. Des. Dev. 10 (1971) 541.
[29] D. Chatterjee, O. Deutschmann, J. Warnatz, Faraday Discuss. 119 (2001) 371.
[30] F. Rohr, S.D. Peter, E. Lox, M. Kögel, A. Sassi, L. Juste, C. Rigaudeau, G. Belot, P. Gelin, M. Primet, Appl. Catal. B 56 (2005) 201.
[31] I. Aartun, H.J. Venvik, P. Pfeifer, O. Görke, K. Schubert, Catal. Today 110 (2005) 98.
[32] A.A. Davydov, Infrared Spectroscopy of Adsorbed Species on the Surface of Transition Metal Oxides, John Wiley, New York, 1990.
[33] K. Nakamoto, Infrared and Raman Spectra of Inorganic and Coordination Compounds, John Wiley, New York, 1997.
[34] P.J. Levy, V. Pitchon, V. Perrichon, M. Primet, M. Chevrier, C. Gauthier, J. Catal. 178 (1998) 363.
[35] T. Finke, M. Hartmann, M. Gernsbeck, U. Eisele, C. Vincent, S. Kureti, H. Bockhorn, Thermochim. Acta 473 (2008) 32.
[36] O. Deutschmann, Habilitation Thesis, University of Heidelberg, 2001.
[37] W.H. Weinberg, R.M. Lambert, C.M. Comrie, J.W. Linnett, Surf. Sci. 30 (1972) 299.
[38] L. Olsson, B. Westerberg, H. Persson, E. Fridell, M. Skoglundh, B. Andersson, J. Phys. Chem. B 103 (1999) 10433.
[39] K. Christmann, Introduction to Surface Physical Chemistry, Springer, New York, 1991.
[40] C.T. Campbell, G. Ertl, H. Kuipers, J. Segner, Surf. Sci. 107 (1981) 220.
[41] L. Olsson, H. Persson, E. Fridell, M. Skoglundh, B. Andersson, J. Phys. Chem. B 105 (2001) 6895.
[42] N. Apostolescu, T. Schröder, S. Kureti, Appl. Catal. B 51 (2004) 43.
[43] C.N. Costa, A.M. Efstathiou, J. Phys. Chem. B 108 (2004) 2620.
[44] S. Kuba, Ph.D. Thesis, University Ludwig Maximilian of Munich, 2001.
[45] T. Davidian, N. Guilhaume, E. Iojoiu, H. Provendier, C. Mirodatos, Appl. Catal. B 73 (2007) 116.